Topology of rotating stratified fluids with and without background shear flow

Ziyan Zhu [1,*] Christopher Li [2] and J. B. Marston [3]

[1]*Stanford Institute for Materials and Energy Sciences, SLAC National Accelerator Laboratory, Menlo Park, California 94025, USA*

[2]*Department of Physics, Brown University, Providence, Rhode Island 02912-1843, USA*

[3]*Brown Theoretical Physics Center and Department of Physics, Brown University, Providence, Rhode Island 02912-1843, USA*

(Received 19 February 2022; accepted 31 August 2023; published 15 September 2023)

Poincaré inertio-gravity modes described by the shallow water equations in a rotating frame have nontrivial topology, providing a perspective on the origin of equatorially trapped Kelvin and Yanai waves. We investigate the topology of rotating shallow water equations and continuously stratified primitive equations with and without background shear flow. Continuously stratified fluids support waves that are analogous to the edge modes of weak three-dimensional topological insulators. Background shear flow not only breaks the Hermiticity and homogeneity of the system but also leads to instabilities. By introducing a gauge-invariant winding number, we show that singularities in the phase of the Poincaré waves of the unforced shallow-water equations and primitive equations persist in the presence of both horizontal and vertical shear flows. Thus, the bulk Poincaré bands have nontrivial topology and we expect and confirm the persistence of the equatorial waves in the presence of shear along the equator where the Coriolis parameter f changes signs.

DOI: 10.1103/PhysRevResearch.5.033191

I. INTRODUCTION

Oceanic and atmospheric waves share fundamental physics with topological insulators and the quantum Hall effect, and topology plays an unexpected role in the movement of the atmosphere and ocean fluids [1]. Topology guarantees the existence of unidirectional propagating equatorial waves on planets with atmospheres or oceans. In particular, there is a topological origin for two well-known equatorially trapped waves, the Kelvin and Yanai modes, caused by the breaking of time-reversal symmetry by planetary rotation. Coastal Kelvin waves have also been demonstrated to have a topological origin [2]; thus Kelvin's 1879 discovery of such waves [3] likely marked the first time that edge modes of topological origin were uncovered in any context (though the topological nature remained hidden). Recently, reanalysis observations of Poincaré-gravity waves in the stratosphere have been used to demonstrate the nontrivial topology of these waves [4]. In light of these discoveries, it is important to consider the generalization of the shallow water equations to the more general problem of continuously stratified fluids. At the same time, it is also crucial to consider fluids driven by shear flows and damped by friction. Such extensions bring greater realism to models of actual fluids both on Earth [5] and on other planets [6]. The extension to background shear may also pave the way to the treatment of nonlinearities through the use of the mean-field quasilinear approximation [7–9] that self-consistently treats the interaction of waves with mean flows.

The existence of topological edge modes can be understood, via the principle of bulk-interface correspondence, to be predicted by the nontrivial topology of bulk modes. Bulk-interface correspondence has been invoked for the quantum Hall effect and topological insulators [10,11] as well as for a variety of classical wave systems, including nanophotonics [12–15], acoustics [16–18], mechanical systems [19,20], continuum fluids [1,2,21–23], and plasmas [24–26]. The principle is clearest for Hermitian systems. Driving and dissipation, however, lead to non-Hermitian dynamics [27–31]. By continuity, weak damping and driving may be expected to only change the waves slightly, but what happens as the forcing increases? Efforts have been put into the topological classification of non-Hermitian systems [32–35]. Whether or not bulk-interface correspondence continues to hold remains a central problem. It has been argued that traditional bulk-interface correspondence breaks down in non-Hermitian systems [36,37]. Alternatives to the topological Chern number have been proposed [33,38–41]. Non-Hermitian bulk-interface correspondence has also been explored experimentally [42,43]. Here, we show that the phase singularity in the bulk wave functions persists in the presence of shear flow. The phase of the bulk Poincaré modes exhibits a vortex or antivortex at the origin in the wave-vector space, with a change in the phase winding number across the equator. We show that equatorial Yanai and Kelvin waves persist in the background shear, consistent with the continued applicability of the principle of bulk-interface correspondence in the non-Hermitian realm.

The paper is organized as follows. A brief introduction to topology in the context of fluid systems is presented in Sec. II. It includes references to some pedagogical reviews. We derive

*ziyanzhu@stanford.edu

the shallow water equations in the presence of shear and compare numerical and perturbative methods to find the wave spectrum in Sec. III. The continuously stratified primitive equations with and without shear are analyzed in the f-plane approximation in Sec. IV and the Chern number for each band is found following the procedure introduced in Ref. [1], demonstrating a correspondence with weak 3D topological insulators. In Sec. V, we show that the system is unstable with both horizontal and vertical shear. In Sec. VI, we numerically calculate the winding number to demonstrate the topology of the bulk. We first show that bulk-interface correspondence holds in the case of spatially varying Coriolis parameters. (The reader may wish to look at Ref. [4], which attempts to make the topological concepts discussed here accessible to climate scientists and geophysical fluid dynamicists.) We then show our main result, which is that bulk-interface correspondence also appears to hold as background shear is turned on and the dynamics become non-Hermitian. Discussion and concluding remarks are made in Sec. VII. Some details of the calculations are relegated to the Appendices.

II. TOPOLOGICAL INVARIANTS AND BULK-INTERFACE CORRESPONDENCE

Topology is the branch of mathematics concerned with the qualitative shapes of objects that remain unchanged under continuous deformations. The topological equivalence of a donut and a coffee mug (both have a single hole) is a commonly mentioned example, as is the fact that an Möbius strip cannot be made orientable without tearing the paper and that it is impossible to comb the spines of a hedgehog (the hairy ball theorem).

Topology finds noteworthy applications in fluids. Vortex rings, for instance, show persistence that is rooted in topology. The persistence of vortex rings was striking enough for William Thomson (Lord Kelvin) to attempt to develop a theory of atoms based upon vortex rings in the hypothetical aether. Kelvin's circulation theorem states that the circulation (the line integral of the fluid velocity) around a closed loop that is advected with the fluid and thus deformed by the internal motion remains constant in the absence of viscosity and forcing. Tornadoes, hurricanes, Jupiter's red spot, and even cutoff low-pressure regions in Earth's atmosphere and vortex loops in the ocean are all examples of persistent vortices.

Topology may also be applied to more abstract mathematical spaces. In work recognized by the 2016 Nobel Prize in Physics, David Thouless and his collaborators demonstrated that the quantized conductance of the integer quantum Hall effect can be understood mathematically in terms of the topology of complex-valued wave functions that live on a compact Brillouin zone [44]. The electrical Hall conductance is proportional to an integer Chern number that characterizes the topology of the wave functions. This quantization has a physical interpretation as electrical currents that propagate around the boundary of the semiconducting material in discrete modes, modes that owe their existence to the principle of bulk-interface correspondence. The principle states that nontrivial topology away from a boundary implies the existence of unidirectional waves trapped along the boundary. The quantum of resistance, h/e^2, can be measured so precisely that it has now been adopted as the international standard of resistance.

The topology of linearized wave equations is frequently quantified in terms of the Chern number [45]. See Refs. [4,46–48] for some pedagogical reviews. However, the Chern number has a number of drawbacks. In contrast to systems on spatial lattices (where the Chern number was first applied), for continuous systems such as fluids the Chern number need not be integer valued as it depends on how an integral over the Berry curvature is regularized at high wave vectors. This ambiguity can sometimes be avoided by compactification [1,2]. Our viewpoint here is that this is more of a mathematical problem than a physical one because at small scales dissipation becomes strong providing a natural (albeit non-Hermitian) regularization at high wave numbers. Ultimately, at the smallest scales, the fluid description passes over to Hamiltonian molecular dynamics. It is unclear how to extend the Chern number to systems with dissipation, driving, or nonlinearities—all properties of real fluids.

By contrast, these ambiguities do not arise for a winding number invariant. To demonstrate the concept of the winding number, it is necessary to define the gauge-invariant, complex-valued quantity Ξ in the frequency-wave-vector space for a given eigenmode,

$$\Xi_n(k_x, k_y) \equiv h_n^*(k_x, k_y)\, v_n(k_x, k_y), \tag{1}$$

where h is the height, v is the meridional velocity, and n is an eigenmode index. Note that the frequency depends on (k_x, k_y) and n. Normal wave modes, which are defined only up to an overall phase and magnitude, have their overall phases cancel out in Eq. (1), leaving only the relative phase difference between h and v and making Ξ gauge invariant.

The idealized rotating shallow-water model on the f plane is an illustration of the winding number. Figure 1 shows the positive and negative frequency Poincaré modes (inertio-gravity waves) and the zero-frequency geostrophically balanced mode. The geostrophically balanced mode becomes Rossby waves if the Coriolis parameter varies with latitude. The topology of Poincaré-gravity modes is characterized by a vortex or antivortex in the frequency-wave-vector space, with winding number ± 1. A winding number of $+1$ means Ξ increases (decreases) by 2π as one moves around the center of the vortex in a clockwise (counterclockwise) sense. On the other hand, the winding number of the geostrophic balanced mode is 0 (topologically trivial). The winding number, as an alternative to the Chern number, serves the same function by quantifying the topology of the bands.

A band inversion is a phenomenon where the winding number flips sign. This can occur for the Poincaré-gravity waves when either the Coriolis parameter or the wave frequency changes signs. According to the bulk-interface correspondence, the number of waves that traverse the otherwise forbidden region in the frequency space is the change in the winding number, which is two in this case.

Spectral flow in frequency-wave-vector space as the zonal wave number increases shows that the negative frequency Poincaré band loses two modes, the geostrophic band gains and loses one mode, and the positive frequency Poincaré band gains the two modes. These are the equatorial Kelvin and Yanai waves (the Yanai waves are also called mixed

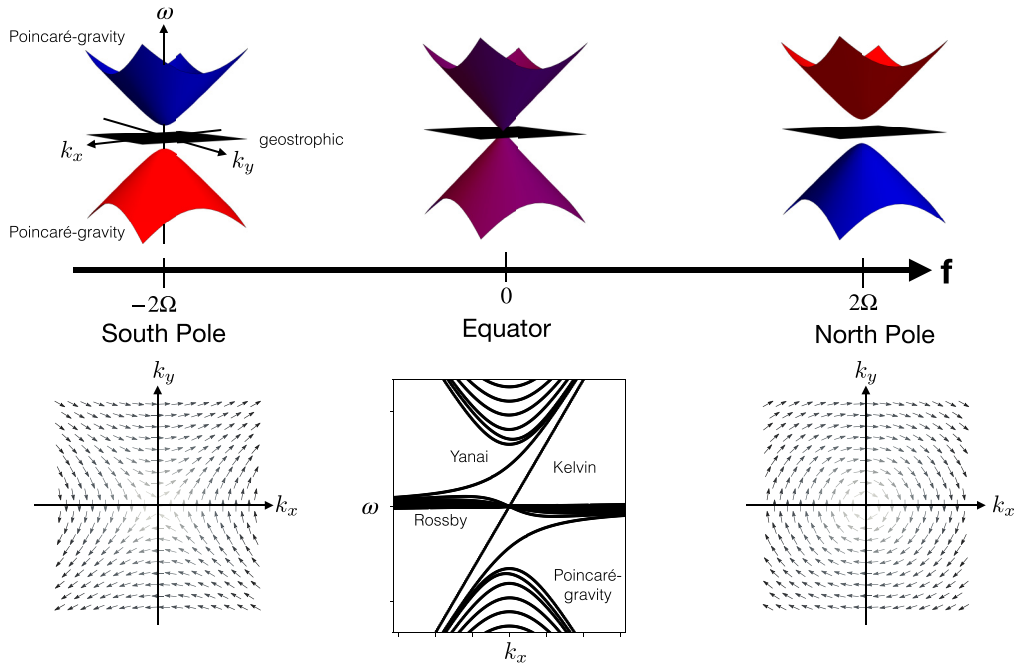

FIG. 1. Dispersion relation in frequency-wave-vector space of the rotating shallow water equations in the f-plane approximation as a function of latitude. The upper and lower bands are positive and negative frequency modes of the Poincaré waves, and the color indicates the sign of the winding number of the upper band (blue $= -1$, red $= +1$) as shown by the plots of the argument of $\Xi(k_x, k_y)$ in the lower half of the figure (see text). At the equator $f = 0$, the frequency gap vanishes in a Weyl point and a topological transition occurs (purple) as the two bands invert. The subinertial range has only a zero-frequency band (black) containing modes in exact geostrophic balance. The inset shows the dispersion relation on the equatorial β plane with the quasigeostrophic Rossby waves, the Poincaré waves, and the unidirectional Kelvin and Yanai waves. The vector plot corresponds to the south pole (left) and the north pole (right), respectively. (Figure and caption adapted from Ref. [4].)

Rossby-gravity waves). The two equatorial modes move with an eastward group velocity at all zonal wave numbers, and this unidirectional propagation is a consequence of the breaking of time-reversal invariance by the planetary rotation.

III. ROTATING SHALLOW WATER EQUATIONS WITH HORIZONTAL SHEAR

We begin this section by presenting the linearized rotating shallow water equations in the presence of horizontal shear and later consider vertical shear in the continuously stratified primitive equations. (See Chap. 5, "Zonally symmetry wave—mean interaction theory," of Ref. [49] for relevant background.) Note that x and y are zonal and meridional coordinates, respectively. For simplicity, we only consider shearing flow moving in the x direction: $\boldsymbol{U}(y) = (U(y), 0)$. We first introduce the following dimensionless quantities:

$$\tilde{t} = 2\Omega t, \quad \tilde{\eta} = \frac{\eta}{H}, \quad \tilde{H}(y) = 1 + \frac{h(y)}{H}, \quad \tilde{\boldsymbol{u}} = \frac{\boldsymbol{u}}{c},$$
$$\boldsymbol{U} = \frac{U}{c}, \quad \tilde{f}(y) = \frac{f(y)}{2\Omega}, \quad \tilde{\boldsymbol{x}} = \frac{\boldsymbol{x}}{L_d}, \tag{2}$$

where $c = \sqrt{gH}$ is the gravity waves speed in nonrotating shallow water equations, Ω is the planet rotation rate, H is the zonally averaged depth in the absence of shear, and $L_d = c/2\Omega$ is the global Rossby radius of deformation. Note that we assume L_d is much smaller than the domain width, which allows us to treat the two equators independently. In terms of these nondimensionalized quantities and dropping the tildes for clarity, the shallow water equations after linearization and nondimensionalization are given as follows (see Appendix A for the derivation):

$$\begin{aligned} \partial_t u + U(y)\partial_x u + v\partial_y U(y) + \partial_x \eta - f(y)v = 0, \\ \partial_t v + U(y)\partial_x v + \partial_y \eta + f(y)u = 0, \\ \partial_t \eta + H(y)(\partial_x u + \partial_y v) + v\partial_y H(y) + U(y)\partial_x \eta = 0, \end{aligned} \tag{3}$$

where u, v are, respectively, the x and y components of fluid velocity in the horizontal directions, $f(y)$ is the Coriolis parameter, $H(y)$ is the mean layer depth and η is the fluctuation in the depth about this mean; thus the total layer depth is given by $h = H(y) + \eta$. Note that H here is a function of y due to the balance with the horizontal shear flow [see Eq. (5) below].

We now further specialize to the case of a background basic shear flow that oscillates sinusoidally in the y direction:

$$U(y) = U_0 \sin\left(\frac{2\pi y}{\Lambda}\right), \tag{4}$$

where U_0 is the magnitude of the shear flow measured in units of $c \equiv \sqrt{gh}$ and Λ is the wavelength of the shear. Note that linear shear $U(y) \propto y$ is incompatible with the periodic boundary conditions that we adopt in the following to eliminate any boundaries from the bulk problem that would confuse the application of the bulk-interface correspondence principle, as the only boundaries that we consider here are those located where the Coriolis parameter vanishes. Geostrophically balancing the basic flow then determines the mean depth $H(y)$,

which satisfies

$$\frac{\partial H(y)}{\partial y} = -f(y)U(y). \tag{5}$$

In the f-plane approximation, $f(y) = f_0$ for a constant f_0 and the mean depth is

$$H(y) = 1 + \frac{U_0 f_0 \Lambda}{2\pi} \cos\left(\frac{2\pi y}{\Lambda}\right). \tag{6}$$

A. Waves on a planet with two equators

To investigate whether or not bulk-interface correspondence continues to hold in the presence of horizontal shear, we first examine the dispersion relation of shallow water waves in the presence of both rotation and shear. The wave frequencies are found numerically with the open-source pseudospectral DEDALUS package [50]. We employ $N_y = 61$ spectral modes in the y direction, sufficient to resolve the waves and odd in number so symmetry about $y = 0$ can be preserved. We check that increasing the resolution N_y does not change the frequencies significantly, including the Rossby wave frequency and the dispersion of the geostrophic modes. We choose

$$f(y) = \sin\left(\frac{2\pi y}{L_y}\right) \tag{7}$$

and set $L_y = 4\pi$, where L_y is the width of the periodic domain (Fig. 2). This choice respects the periodic boundary conditions and is sometimes called a planet with two equators as the Coriolis parameter changes signs twice across the domain [1].

Assuming the sinusoidal horizontal shear Eq. (4), which is antisymmetric about the equator located at $y = 0$, has the same periodicity as the domain size ($\Lambda = L_y$), the mean depth is

$$H(y) = 1 + U_0\left[\frac{L_y}{8\pi}\sin\left(\frac{4\pi y}{L_y}\right) - \frac{y}{2}\right]. \tag{8}$$

Similarly, if the shear is symmetric about the equator at $y = 0$, namely,

$$U(y) = U_0 \cos\left(\frac{2\pi y}{\Lambda}\right), \tag{9}$$

from geostrophic balance, the mean depth is

$$H(y) = 1 + \frac{U_0 L_y}{8\pi}\cos\left(\frac{4\pi y}{L_y}\right). \tag{10}$$

We consider both profiles in the following.

In the absence of shear, Fig. 2(a), equatorial Kelvin waves and Yanai waves appear in the gap between the high-frequency Poincaré and low-frequency planetary waves. These waves have a topological origin [1]. They propagate unidirectionally (their group velocity does not change sign for all k_x), as guaranteed by topology. Note that while the wave crest of the Rossby wave indeed always has a westward component, its group velocity can be both directions, as can be seen from the wave dispersion in Fig. 2(a). As there are two oppositely oriented equators, there are both eastward and westward propagating modes localized respectively at each equator. When shear $U_0 \neq 0$ is turned on, the planetary Rossby waves are Doppler shifted and we observe continuous spectra near the zero frequency [51]. The continuous spectrum spans $\omega = \pm U_0 k_x$. The dispersion of the Poincaré modes also changes with increasing k_x; see Figs. 2(b) and 2(c). The Kelvin and Yanai waves remain localized near the equators. We have also investigated spectra with larger values of U_0 and find that the Kelvin and Yanai waves persist so long as U_0 is not too large. If U_0 is too large, the bulk bands and the boundary modes become difficult to distinguish due to significant changes in the frequency of the bulk modes and the large Doppler shift of the planetary waves, especially in the case of the sine shear flow. We show below that the continued

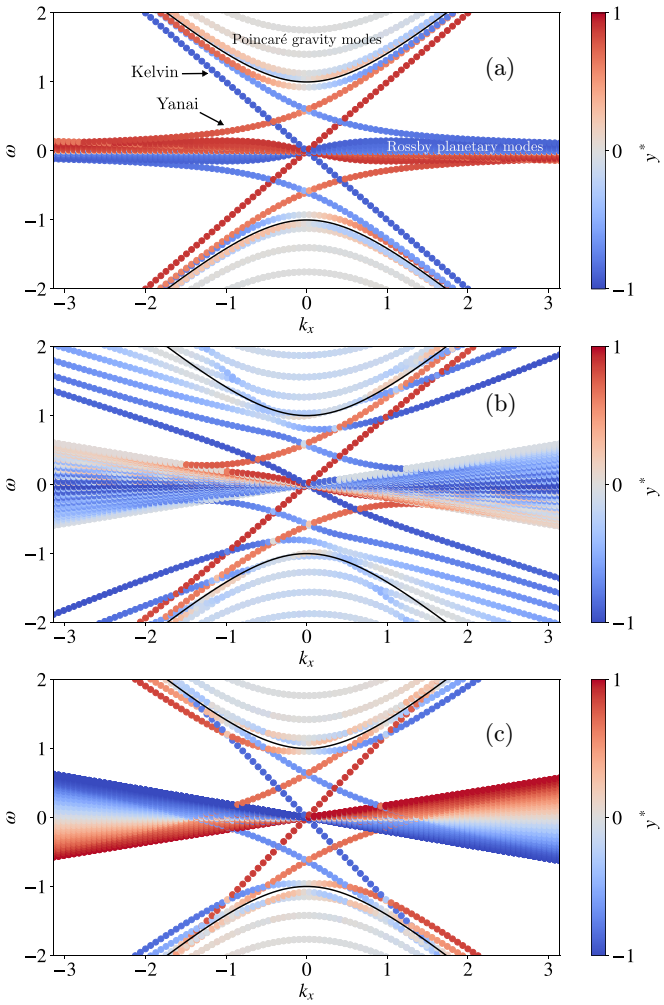

FIG. 2. Numerical evaluation of the frequency-wave-number dispersion of the linearized shallow water equations obtained with DEDALUS with $N_y = 61$ spectral modes showing the spectral flow of the Kelvin and Yanai waves between bands. Colors show the projected real space position and $y^* = \langle\Psi|y|\Psi\rangle/L_y$. (a) No shear. (b) Imposed sine shear [Eq. (4)] with $U_0 = 0.2$, and (c) cosine shear [Eq. (9)] with $U_0 = 0.2$. The Coriolis parameter varies sinusoidally [Eq. (7)] and changes signs at $y = 0$ ($y^* = -1$) and $y = \pm L_y/2$ ($y^* = 1$). We set $L_y = 4\pi$. Black solid lines represent the frequency of the $k_y = 0$ Poincaré modes in the absence of shear and in the f-plane approximation: $f = 1$: $\omega = \pm\sqrt{k_x^2 + f^2}$.

presence of the waves is consistent with the persistence of bulk-interface correspondence in the presence of shear.

B. Bulk waves on the *f* plane

We now develop a purely spectral approach to include shear that is amenable to either direct diagonalization or a perturbative expansion. First, we briefly review shallow water waves on the f plane in the absence of shear flow [1]. We expand the eigenmodes in the plane wave basis, $(u, v, \eta) = \Psi(k_x, k_y, f_0) = \hat{\Psi}\exp(ik_x x + ik_y y - i\omega t)$. In this basis, the linear wave operator is a 3×3 matrix:

$$L_0(k_x, k_y, f_0) = \begin{pmatrix} 0 & if_0 & k_x \\ -if_0 & 0 & k_y \\ k_x & k_y & 0 \end{pmatrix}. \tag{11}$$

The amplitudes of the normal modes $\Psi_{\pm,0}(k_x, k_y, f_0)$ with frequencies $\omega_{\pm,0}$ can be obtained by diagonalizing L_0. The positive Poincaré mode frequency is $\omega_+ = \sqrt{k_x^2 + k_y^2 + f_0^2}$ with the eigenmode,

$$\Psi_+ = \begin{pmatrix} -\frac{k_x}{k} + i\frac{f_0 k_y}{k\sqrt{k^2+f_0^2}} \\ \frac{k_y}{k} - i\frac{f_0 k_x}{k\sqrt{k^2+f_0^2}} \\ \frac{k}{\sqrt{k^2+f_0^2}} \end{pmatrix}, \tag{12}$$

where $k \equiv \sqrt{k_x^2 + k_y^2}$. A highly degenerate geostrophically balanced mode appears at zero frequency, $\omega_0 = 0$ (the degeneracy is lifted when the Coriolis parameter varies with latitude or in the presence of shear):

$$\Psi_0(k_x, k_y, f_0) = \frac{1}{\sqrt{k^2 + f_0^2}} \begin{pmatrix} -ik_y \\ ik_x \\ f_0 \end{pmatrix}. \tag{13}$$

Finally, the negative Poincaré mode has angular frequency $\omega_- = -\omega_+$ with corresponding wave function $\Psi_-(k_x, k_y, f_0) = \Psi_+(-k_x, -k_y, -f_0)$, reflecting the fact that the wave amplitudes in real space are real valued.

For Poincaré-gravity waves, the gauge-invariant quantity displays a vortex or antivortex (depending on the signs of the frequency and the Coriolis frequency) centered at the origin in wave-vector space,

$$\Xi_\pm(k_x, k_y) = \frac{k_y - i\,\mathrm{sgn}(f_0)k_x}{f_0}, \tag{14}$$

where we use the long-wavelength approximation $k^2 \ll f_0^2$. The vortex (antivortex) has winding number ±1, which constitutes its topological charge. Representing the phase of Ξ with an arrow makes these patterns evident, as shown in Fig. 1. The zero-frequency geostrophic mode, by contrast, has in the same limit

$$\Xi_0(k_x, k_y) = \frac{ik_x}{f_0}, \tag{15}$$

and thus has a domain wall at $k_x = 0$ and zero winding number. Its topological charge therefore vanishes.

C. Horizontal shear flow on the *f* plane

In the presence of shear flow, the system is no longer translationally invariant along the y direction. While the linear wave operator can still be expressed as a matrix in wave-vector space, it is no longer composed of 3×3 block matrices along the diagonal. We first rewrite Eqs. (3) in position space in the form of a matrix of differential operators:

$$\hat{L}(x, y, f_0, U_0) = i\begin{pmatrix} U(y)\partial_x & \frac{\partial U(y)}{\partial y} - f_0 & \partial_x \\ f_0 & U(y)\partial_x & \partial_y \\ H(y)\partial_x & H(y)\partial_y - \frac{\partial H}{\partial y} & U(y)\partial_x \end{pmatrix}. \tag{16}$$

This linear operator preserves the parity-time (PT) symmetry despite the broken Hermiticity, and spontaneous PT-symmetry breaking has been known to lead to instabilities [52,53]. However, note that if the shear flow has dependence on both x and y (i.e., $U(x, y)$), PT symmetry would be broken. Substituting in the sine shear flow $U(y)$ from Eq. (4) with $H(y)$ satisfying the geostrophic balance in Eq. (5), we obtain

$$\hat{L}(x, y, f_0, U_0) = i\begin{pmatrix} U_0 \sin\left(\frac{2\pi y}{\Lambda}\right)\partial_x & \frac{2\pi U_0}{\Lambda}\cos\left(\frac{2\pi y}{\Lambda}\right) - f_0 & \partial_x \\ f_0 & U_0 \sin\left(\frac{2\pi y}{\Lambda}\right)\partial_x & \partial_y \\ \left[1 + \frac{U_0 f_0 \Lambda}{2\pi}\cos\left(\frac{2\pi y}{\Lambda}\right)\right]\partial_x & \left[1 + \frac{U_0 f_0 \Lambda}{2\pi}\cos\left(\frac{2\pi y}{\Lambda}\right)\right]\partial_y - U_0 f_0 \sin\left(\frac{2\pi y}{\Lambda}\right) & U_0 \sin\left(\frac{2\pi y}{\Lambda}\right)\partial_x \end{pmatrix}. \tag{17}$$

Note that the linear wave operator has a y dependence, which means that when expanding H in wave-vector space, different modes with different k_y's can mix. Without loss of generality, we assume $\Lambda = 1$. We can consider the simplest case where there are only three modes, k_y, $k_y \pm 2\pi$, in the basis. In this case, the full linear wave operator is a 9×9 matrix that can be decomposed into 3×3 blocks, which can be formally represented as follows:

$$\mathcal{L}_{9\times9}(k_x, k_y, f_0, U_0) = \begin{pmatrix} L_0(k_x, k_y + 2\pi, f_0) & T_1(k_x, k_y, f_0, U_0) & 0 \\ T_2(k_x, k_y + 2\pi, f_0, U_0) & L_0(k_x, k_y, f_0) & T_1(k_x, k_y - 2\pi, f_0, U_0) \\ 0 & T_2(k_x, k_y, f_0, U_0) & L_0(k_x, k_y - 2\pi, f_0) \end{pmatrix}, \tag{18}$$

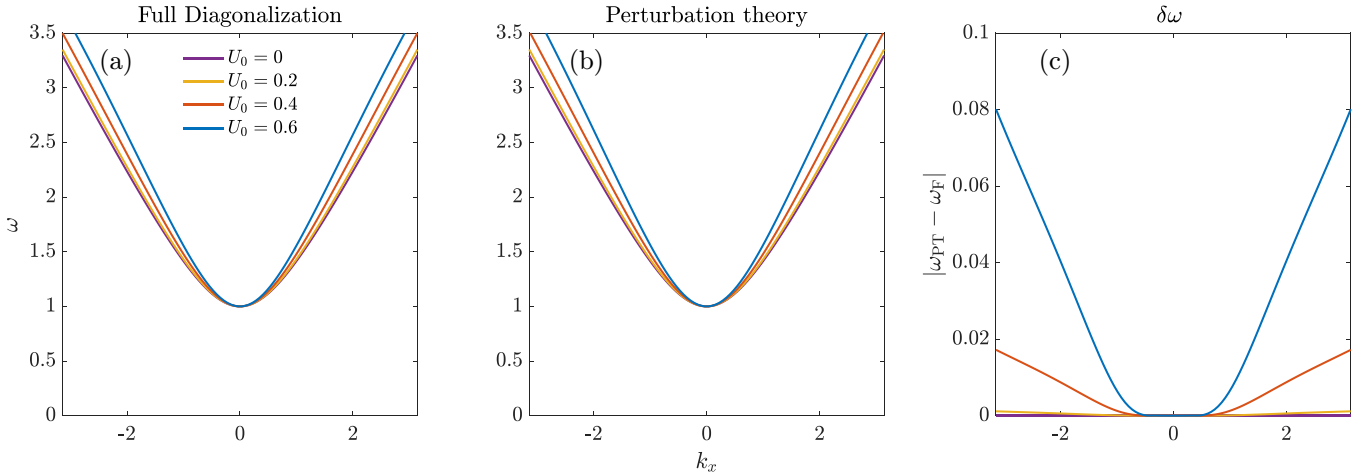

FIG. 3. Comparison of the frequency of the lowest positive frequency Poincaré modes from (a) full diagonalization and (b) perturbation theory of the 9×9 linear wave operator. (c) The difference between the two frequencies in (a) and (b).

where L_0 is given in Eq. (11) and T_1 and T_2 are the transition matrices between modes:

$$T_1(k_x, k_y, f_0, U_0) = \langle k_x, k_y + 2\pi|\hat{L}|k_x, k_y\rangle = \frac{U_0}{2}\begin{pmatrix} ik_x & 2\pi i & 0 \\ 0 & ik_x & 0 \\ \frac{f_0 k_x}{2\pi} & \frac{k_y f}{2\pi} + f_0 & ik_x \end{pmatrix},$$

$$T_2(k_x, k_y, f_0, U_0) = \langle k_x, k_y - 2\pi|\hat{L}|k_x, k_y\rangle = \frac{U_0}{2}\begin{pmatrix} -ik_x & 2\pi i & 0 \\ 0 & -ik_x & 0 \\ \frac{f_0 k_x}{2\pi} & \frac{k_y f_0}{2\pi} - f_0 & -ik_x \end{pmatrix}. \quad (19)$$

The derivation of T_1 and T_2 can be found in Appendix B. The matrix $T_1(k_x, k_y, f_0, U_0)$ connects wave number k_y to $k_y + 2\pi$ and $T_2(k_x, k_y, f_0, U_0)$ connects k_y to $k_y - 2\pi$. Note that $T_1 \neq T_2^\dagger$ and the linear wave operator is non-Hermitian. The frequency spectrum and the eigenvectors can then be obtained by diagonalizing the full matrix $\mathcal{L}(k_x, k_y, f_0, U_0)$. We validate our results by comparing our spectra with the ones obtained with DEDALUS [50] in Appendix C.

D. Perturbative treatment of shear

We also consider a perturbative expansion of the eigenfunctions (values) in powers of the shear [54–56]. We may treat the shear flow perturbatively by considering the quantity $\delta\mathcal{L} = \mathcal{L} - \mathcal{L}_0$, namely, the off-diagonal blocks in Eq. (18). The correction to the frequency of the Poincaré mode first appears at second order in the shear:

$$\omega_n = \omega_n^{(0)} + \sum_{m\neq n} \frac{\delta\mathcal{L}_{nm}\delta\mathcal{L}_{mn}}{\omega_n^{(0)} - \omega_m^{(0)}}, \quad (20)$$

where $\delta\mathcal{L}_{mn} = \langle m|\delta\mathcal{L}|n\rangle$, and m and n are indices that label a wave-vector state with some k_y. The wave functions including the first-order correction are given as follows:

$$|n\rangle = |n^{(0)}\rangle + \sum_{m\neq n} \frac{\delta\mathcal{L}_{mn}}{\omega_n^{(0)} - \omega_m^{(0)}}|m^{(0)}\rangle, \quad (21)$$

where $|n^{(0)}\rangle$ and $|m^{(0)}\rangle$ are unperturbed wave functions corresponding to some k_y. The perturbed eigenmodes are still labeled by wave vector (k_x, k_y) despite the fact that they contain contributions from modes at other k_y. To second order in the shear U_0, the frequencies only involve intermediate modes at wave vectors $(k_x, k_y \pm 2\pi)$; higher orders of perturbations involve increasing departures of the wave number away from $k_x = 0$. Figure 3 compares the frequency obtained from full diagonalization of the 9×9 linear wave operator to the spectrum from second-order perturbation theory. The two spectra agree well with each other. Through comparing the perturbative spectrum and the full diagonalization, we show that, first, the bulk can be classified by (k_x, k_y) and, second, the change of the bulk Poincaré wave is smooth as a function of U_0. Therefore, we argue that using the bulk-interface correspondence is valid despite the broken Hermiticity. As discussed later in Sec. VI, the first- and second-order perturbative corrections to the wave functions do not alter their topological properties.

E. Wave dynamics

Figures 4 and 5 show snapshots of the propagation of wave number 2 ($k_x = 4\pi/L_x$) Kelvin and Yanai waves subjected to sine and cosine shear. The waves remain localized near the $y = 0$ equator as they propagate. The wave amplitude grows in time with the sine shear [Figs. 4(b) and 4(d)] and decays in time with the cosine shear [Figs. 5(b) and 5(d)], consistent with the imaginary part of the frequency eigenvalues that correspond to growth and decay, respectively, for the two types of the shear. Note that since the sine shear is odd in y, the Kelvin wave also becomes asymmetric in y as time evolves [Fig. 4(b)].

IV. PRIMITIVE EQUATIONS WITH AND WITHOUT SHEAR

We turn next to the continuously stratified primitive equations. It has been shown that nonrotating stratified fluids with profiles of stratification that transition with increasing depth

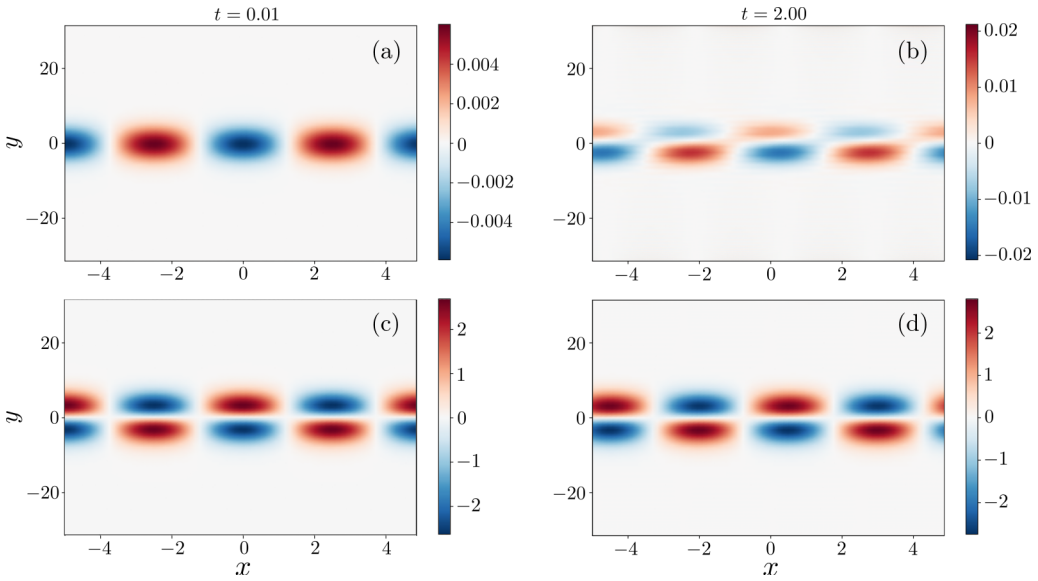

FIG. 4. Time evolution of the η-component of (a), (b) the Kelvin wave and (c), (d) the Yanai wave for sine shear with $U_0 = 0.1$, $N_y = 121$, $N_x = 71$, $L_y = 20\pi$, $L_x = 10$.

from marginally unstable to stable have a wave of topological origin along the interface [57]. We make the standard Boussinesq approximation, and the vertical velocity or variation in the buoyancy replaces the depth as one of the dynamical fields.

We first analyze the topological character of the linear stratified equations in the absence of shear by calculating the topological invariant within the bulk f-plane approximation. The linearized and nondimensionalized equations can be derived from the underlying hydrostatic equations (see Appendix D for the detailed derivation):

$$\begin{aligned}
\frac{\partial u}{\partial t} &= -U(y)\frac{\partial u}{\partial x} - v\frac{\partial U(y)}{\partial y} + f(y)v - \frac{\partial \eta}{\partial x},\\
\frac{\partial v}{\partial t} &= -f(y)u - U(y)\frac{\partial v}{\partial x} - \frac{\partial \eta}{\partial y},\\
\frac{\partial}{\partial t}\frac{\partial \eta}{\partial z} &= -w - U(y)\frac{\partial^2}{\partial x \partial z}\eta,
\end{aligned} \tag{22}$$

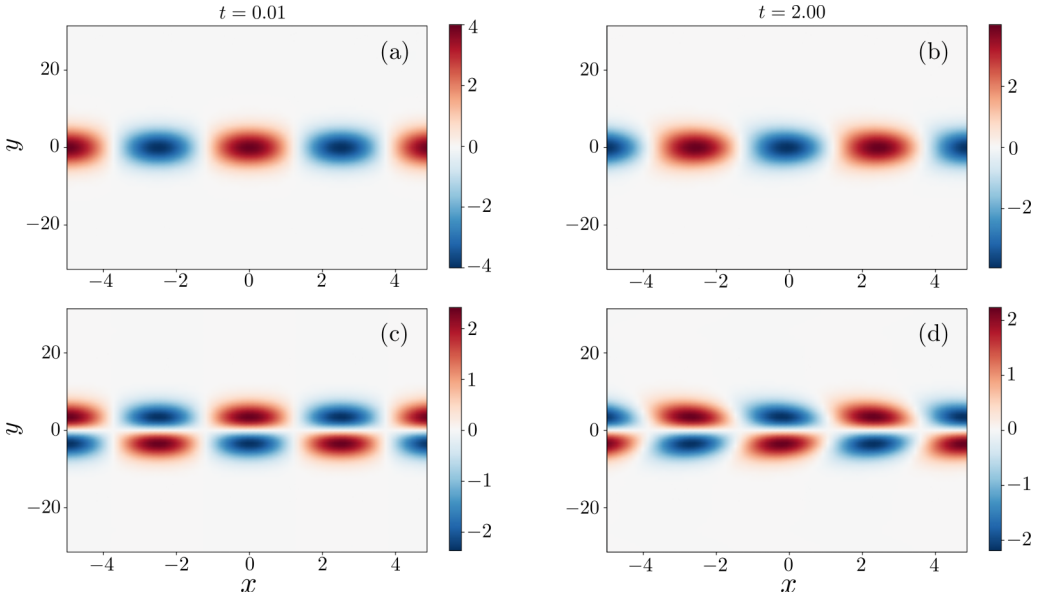

FIG. 5. Time evolution of the η component of (a), (b) the Kelvin wave and (c), (d) the Yanai wave for cosine shear with $U_0 = 0.1$, $N_y = 121$, $N_x = 71$, $L_y = 20\pi$, and $L_x = 10$.

where w is the vertical velocity and the vertical depth variation η, and the buoyancy b are related by the diagnostic relationship $\partial_z \eta = b$.

On the f plane, it is again natural to switch to a basis of plane waves which decouples the modes with different wave numbers in the z direction, k_z. The incompressibility constraint in this basis takes the form $\nabla \cdot \boldsymbol{u} = i(k_x u + k_y v + k_z w) = 0$, permitting the replacement of w and η with b, u, and v. In the absence of shear, Eqs. (22) now correspond in this basis to the linear wave operator:

$$L_0 = \begin{pmatrix} 0 & if_0 & -i\frac{k_x}{k_z} \\ -if_0 & 0 & -i\frac{k_y}{k_z} \\ i\frac{k_x}{k_z} & i\frac{k_y}{k_z} & 0 \end{pmatrix}. \tag{23}$$

The eigenfrequencies of Eq. (23) are $\omega_\pm = \pm\sqrt{f_0^2 + k^2/k_z^2}$ and $\omega_0 = 0$ with corresponding eigenvectors,

$$\Psi_\pm = \frac{1}{\mathcal{N}_1}\begin{pmatrix} \mp ik_z k_x \sqrt{f_0^2 k_z^2 + k^2} + f_0 k_z^2 k_y \\ \mp ik_z k_y \sqrt{f_0^2 k_z^2 + k^2} - f_0 k_z^2 k_x \\ k^2 k_z \end{pmatrix},$$

$$\Psi_0 = \frac{1}{\mathcal{N}_2}\begin{pmatrix} -k_x k_y \\ k_x^2 \\ f_0 k_x k_z \end{pmatrix}, \tag{24}$$

where $k^2 = k_x^2 + k_y^2$, and $\mathcal{N}_{1,2}$ are normalization constants.

We consider the positive frequency eigenvector at fixed nonzero k_z. Letting $f_z = f_0 k_z$ and dividing Ψ_+ by k_z, we have

$$\Psi_\pm = \frac{1}{\mathcal{N}_3}\begin{pmatrix} \mp ik_x \sqrt{f_z^2 + k^2} + f_z k_y \\ \mp ik_y \sqrt{f_z^2 + k^2} - f_z k_x \\ k^2 \end{pmatrix}, \tag{25}$$

where $\mathcal{N}_3$ is the new normalization constant. The Berry connection is

$$\mathrm{Im}\langle \Psi_+ | \nabla_p | \Psi_+ \rangle = \left(-2f_z k_y \sqrt{f_z^2 + k^2}, 2f_z k_x \sqrt{f_z^2 + k^2}, 0\right), \tag{26}$$

where $\boldsymbol{p} = (k_x, k_y, f_z)$. The result is the same as the Berry connection of the positive Poincaré mode of the shallow water equations [1]. The difference of the Chern number between the two hemispheres, $\Delta C_\pm$, can be calculated analytically by integrating the Berry curvature over the unit sphere in (k_x, k_y, f_z) space. For the Poincaré modes, the difference $\Delta C_\pm = \pm 2$. By bulk-interface correspondence, for each k_z, there are two pairs of boundary Kelvin and Yanai modes (one pair each for the two oppositely oriented equators). These stacks of boundary modes are analogous to the edge modes found in weak three-dimensional topological insulators [45].

With sinusoidal horizontal shear flow, the eigenmodes of Eq. (22) can be obtained by the methods outlined in Sec. III C. The method again shows excellent agreement with the result obtained from DEDALUS (not shown in the paper).

With a vertical shear flow, the primitive equations are modified to be the following:

$$\begin{aligned} \frac{\partial u}{\partial t} &= -U(z)\frac{\partial u}{\partial x} - f(y)v - \frac{\partial \eta}{\partial x}, \\ \frac{\partial v}{\partial t} &= -f(y)u - U(z)\frac{\partial v}{\partial x} - \frac{\partial \eta}{\partial y}, \\ \frac{\partial}{\partial t}\frac{\partial \eta}{\partial z} &= -w - U(z)\frac{\partial^2 \eta}{\partial x \partial z}. \end{aligned} \tag{27}$$

In this paper, we consider a linear vertical shear flow, namely, $U(z) = U_0 z$. We numerically simulated the spectra in the (y, z) space using DEDALUS as shown in Fig. 6 with $U_0 = 0.01$. Similar to Fig. 2, we use a sinusoidal Coriolis parameter $f(y) = \sin(2\pi y/L_y)$ with $L_y = 10\pi$. Both Yanai and Kelvin waves are present at different values of vertical wave number k_z.

V. SHEAR INDUCED INSTABILITY

To investigate the stability of the waves in the presence of horizontal shear, we follow Ref. [58]. Introducing the background potential vorticity $Q(y) = \frac{f(y) - \partial_y U(y)}{H(y)}$, perturbations are bounded if there exists some constant $\alpha \in \mathbb{R}$ such that the following two conditions hold for all $y \in [-\frac{L_y}{2}, \frac{L_y}{2}]$: (i) $[\alpha - U(y)]\,\partial_y Q(y) \geqslant 0$ and $[\alpha - U(y)]^2 \leqslant H(y)$. For the sine horizontal shear flow, condition (ii) can be satisfied, but condition (i) requires that the function $g(U_0, y) = U_0 \sin(2\pi y)$ to be greater or equal to zero over the entire domain, but this condition is violated for any $U_0 \neq 0$. The analysis is similar with a cosine shear. Thus, the bulk modes are always unstable in the presence of horizontal shear. We numerically confirm the instability of the bulk modes by presenting the imaginary part of the frequency spectrum in Fig. 7. When $U_0 \neq 0$, the spectrum has a nonzero imaginary part that grows linearly in U_0 for small shear. The instability is most prominent in the planetary Rossby modes.

In the presence of the linear vertical shear with rigid-lid boundaries, since the derivative of $U(z)$ has the same sign at the upper and lower boundaries, Eady instabilities are present at low wave numbers [5]. We numerically verified the presence of Eady instabilities by simulating the primitive equations and observed that the spectra are unstable at low wave numbers.

Despite the presence of instabilities with both horizontal and shear flows, the gauge-invariant phase is a robust method of quantifying the topological nature of the system.

VI. NUMERICAL CALCULATION OF BULK WINDING NUMBERS

For Hermitian systems, bulk-interface correspondence [10,59] establishes a relationship between the topological invariant, the Chern number of the bulk, and the number of edge modes. It states that that the difference in the number of counterpropagating edge modes equals the difference in the Chern number in two bulk regions that are connected at a boundary: $\Delta C = n_L - n_R$, where n_L and n_R are the number of left-moving and right-moving modes. The Chern number can be calculated analytically for the rotating shallow water

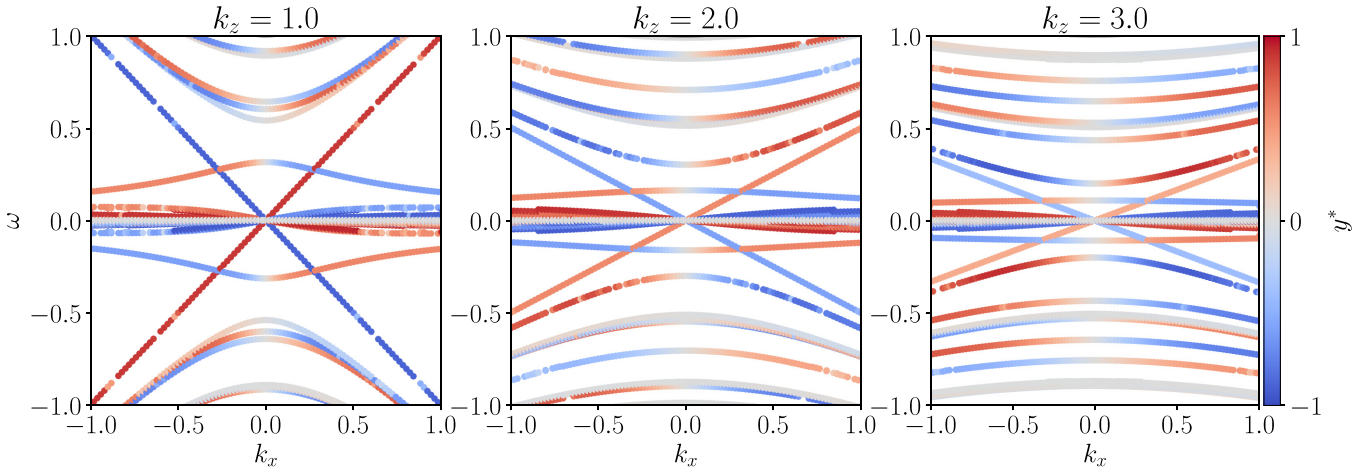

FIG. 6. The spectral flow of Kelvin and Yanai waves between the band gaps exhibited by the linearized primitive equations with a linear vertical shear $U_0 = 0.01$ obtained from DEDALUS with $N_y = 24$, $N_z = 24$, $L_y = 10\pi$, $L_z = 2\pi$ using Fourier basis. The vertical wave number is (a) $k_z = 1$, (b) $k_z = 2$, and (c) $k_z = 3$. The solid black lines are the dispersion relation for the f-plane approximation with $f = 1$, Eq. (24). As in Fig. 2, the color indicates proximity to the two equators. The missing scattered points are due to the difficulty in separating out the modes that correspond to different vertical wave numbers k_z.

equations. Each of the three bands may be parametrized on the unit (k_x, k_y, f) sphere. The Chern number may then be found by integrating the Berry curvature over the surface of the sphere with a fixed radius $\sqrt{k^2 + f^2}$ [1].

In the presence of shear, however, the linear wave operator is no longer Hermitian, and a rigorous bulk-interface correspondence principle is not in hand. We may still investigate the topological properties of the bulk wave functions and compare with the boundary mode spectrum to test whether or not bulk-interface correspondence continues to operate. However, the presence of shear breaks translational invariance in the y direction and the integral of the Berry curvature becomes difficult to evaluate. As an alternative, we instead look for singularities in the phase of the wave functions which appear as vortices in wave-vector space [60]. In the context of

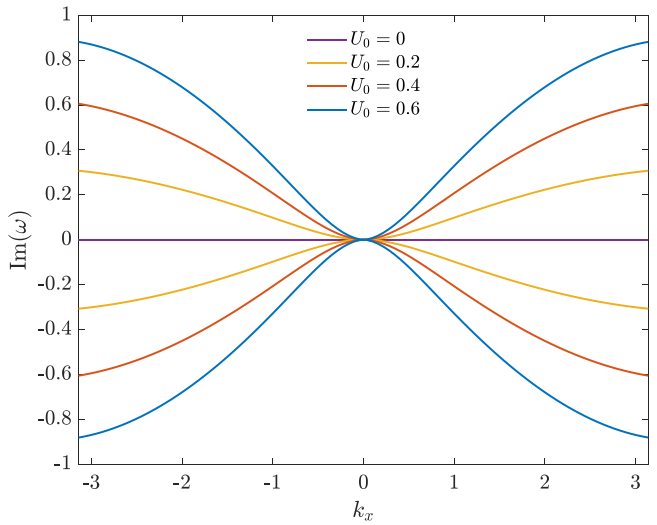

FIG. 7. Imaginary part of the frequency of the lowest-frequency planetary waves obtained from full diagonalization of the 69×69 linear wave operator.

polarization physics, it has been shown that the winding of the polarization azimuth, or the wave-function phase, equals the enclosed Chern number [61,62]. We set the Coriolis parameter such that it is in the bulk (namely, it does not change signs), and examine the phase of the wave functions in (k_x, k_y) to check whether there is a vortex or antivortex in the phase.

A. Spatially varying Coriolis parameter

Delplace *et al.* [1] used an f-plane approximation to analytically calculate the Chern number to show the nontrivial topology of the equatorial waves. However, realistically, Coriolis parameter is a function of the latitude and translational invariance is always broken in the bulk. Here, we first verify that translational invariance in the bulk is not required. To do this, we preserve Hermiticity by considering a spatially varying Coriolis parameter in the absence of the shear flow and find the winding number of the Poincaré modes. We choose

$$f(y) = f_0 + \Delta f \sin\left(\frac{2\pi y}{L_y}\right), \tag{28}$$

so we may adapt the formalism introduced in Eq. (18) to write the linear wave operator in wave-vector space with transition blocks:

$$T_1(\Delta f) = \frac{\Delta f}{2}\begin{pmatrix} 0 & 1 & 0 \\ -1 & 0 & 0 \\ 0 & 0 & 0 \end{pmatrix}, \quad T_2(\Delta f) = T_1(k_x, k_y, \Delta f)^T. \tag{29}$$

By diagonalizing the linear wave operator, we can obtain the spectrum of shallow water equations with the y-dependent $f(y)$. We choose Δf and f_0 such that $f(y)$ does not change sign anywhere; thus we remain in the bulk and no edge modes should arise. Figure 8 shows the bulk spectrum with $\Delta f = 0.5$ and $f_0 = 1$. Frequencies obtained by diagonalization [Fig. 8(a)] in wave-vector space agree with those obtained

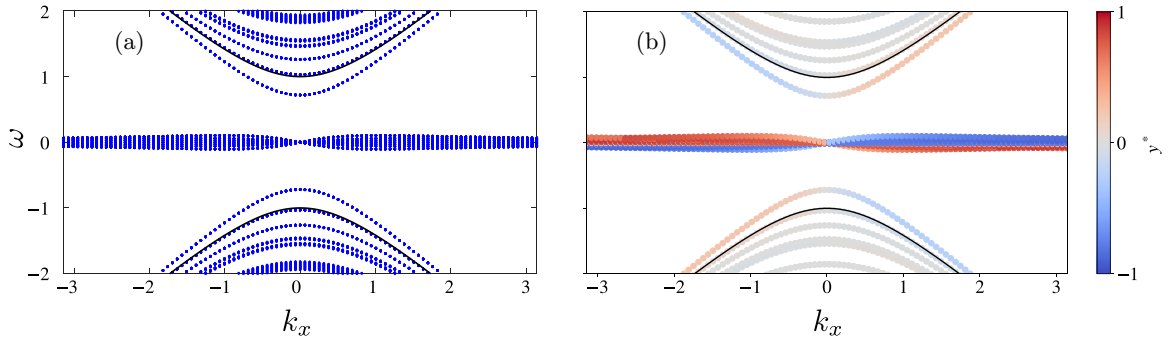

FIG. 8. Numerical calculation of the bulk eigenfrequencies for the spatially varying Coriolis parameter. (a) Diagonalization of the 69×69 wave-vector space linear wave operator. (b) DEDALUS with $N_y = 23$ for $\Delta f = 0.5$, $f_0 = 1$, and $L = 4\pi$. Black dotted lines in (a) and solid lines in (b) represent the frequency of Poincaré modes in the f-plane approximation with $f_0 = 1$: $\omega = \pm\sqrt{k_x^2 + f_0^2}$. Colors in (b) indicate proximity to the two oppositely oriented equators.

with DEDALUS [Fig. 8(b)] and confirm that there are no Kelvin or Yanai waves.

B. Gauge invariant phase

We proceed to calculate the topological index of the bands by searching for singularities in the phase of the frequency eigenfunctions in wave-vector space. The eigenfunctions have gauge freedom, as the phase of the three components can be rotated together by an arbitrary amount $\phi(\boldsymbol{k})$ at each point in wave-vector space:

$$\Psi_{\pm,0}(\boldsymbol{k}) \to e^{i\phi(\boldsymbol{k})}\Psi_{\pm,0}(\boldsymbol{k}). \tag{30}$$

As mentioned previously in Sec. II, we remove the gauge redundancy by multiplying the v component of the Poincaré modes by the complex conjugate of the η component, $\eta^*(\boldsymbol{k}) = \eta(-\boldsymbol{k})$,

$$\Xi_\pm(\boldsymbol{k}) \equiv v_\pm(\boldsymbol{k})\,\eta_\pm(-\boldsymbol{k}), \tag{31}$$

leaving only the internal phase difference between the two amplitudes. Figure 9 depicts the argument of $\Xi_\pm(\boldsymbol{k})$, $\tan^{-1}(\mathrm{Re}(\Xi)/\mathrm{Im}(\Xi))$, of the positive Poincaré modes as a function of k_x and k_y for the spatially varying Coriolis parameter of Eq. (28), where the eigenmodes are obtained by diagonalizing the 69×69 linear operator. The positive Poincaré bands exhibit, respectively, a vortex (winding number 1) and an antivortex (winding number −1) centered at the origin in wave-vector space where the phase cannot be uniquely defined for positive and negative f_0, respectively. The difference in the winding number between the two bands equals 2. The difference in the winding number for either Poincaré band changes by 2 going between the two hemispheres. The planetary waves have no vortex as expected (Fig. 10).

By virtue of the single valuedness of $\Xi_\pm(\boldsymbol{k})$, the winding number must be integer valued and thus topological in character. Unlike the calculation of the Chern number, which is found by integrating the Berry curvature over wave-vector space, no integrals are required for the calculation of the winding number, and the noncompact nature of wave-vector space for continuous fluids does not cloud its interpretation.

The Chern number equals the negative of the total winding within a closed domain, so $\Delta C = \nu_- - \nu_+$, where $\nu_\pm$ is the

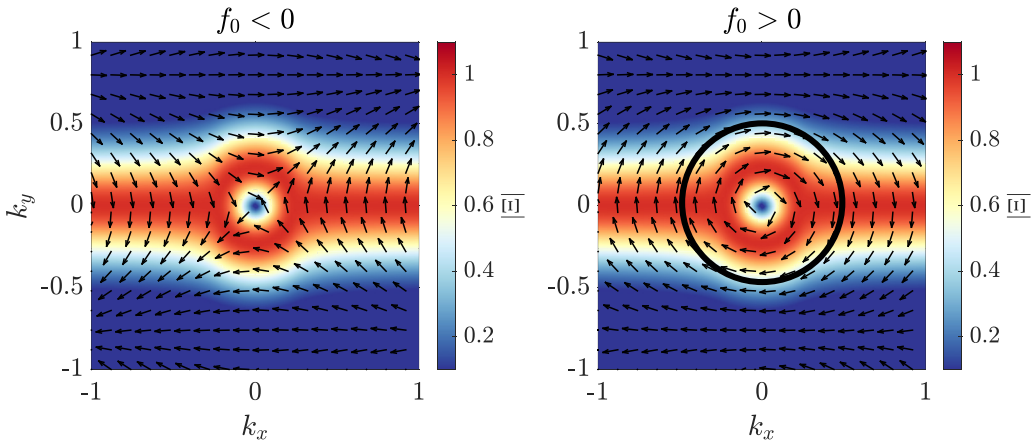

FIG. 9. Arrows representing argument of $\Xi_\pm(\boldsymbol{k}) = v_\pm(\boldsymbol{k})\eta_\pm(-\boldsymbol{k})$ of the lowest positive frequency Poincaré modes as indicated by the direction of the arrows, in the absence of shear but with the sinusoidal Coriolis parameter Eq. (28) with $f_0 = -1$ (left) and $f_0 = 1$ (right), $\Delta f = 0.5$, $\Lambda = 10\pi$, and $L_y \to \infty$. The x and y components of the arrow represent the real and imaginary parts of $\Xi_\pm(\boldsymbol{k})$. The length of the arrows is rescaled to be equal. Colors represent normalized magnitude $|\Xi|$ in arbitrary units. Going in the clockwise direction, the arrows along the black circle smoothly wind by a phase of 2π, suggesting a winding number of 1.

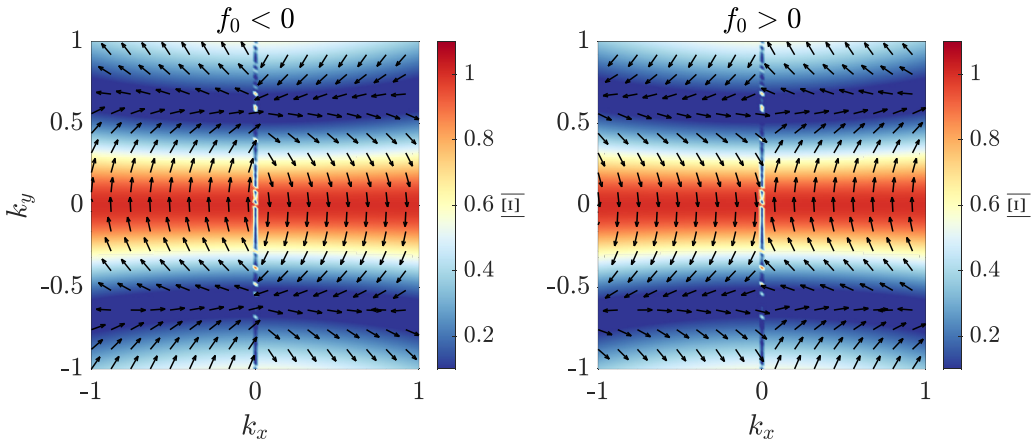

FIG. 10. Same as Fig. 9 but for a Rossby mode in the absence of shear but with the sinusoidal Coriolis parameter Eq. (28) with $f_0 = -1$ (left) and $f_0 = 1$ (right), $\Delta f = 0.5$, $\Lambda = 10\pi$, and $L_y \to \infty$.

winding number of the positive (negative) frequency Poincaré mode and a vortex (antivortex) corresponds to a winding number ± 1 [61]. Thus $\Delta C_+ = -2$ for $f_0 > 0$ and $\Delta C_- = 2$ for $f_0 < 0$, in agreement with the Chern numbers found for the f plane [1]. By bulk-interface correspondence [10,59], the difference in the number of prograde- and retrograde-moving edge modes at the equatorial interface where f changes signs equals the change in the Chern number $\{\Delta C_+, \Delta C_0, \Delta C_-\}$, consistent with the two modes of topological origin localized near each equator. The localized Yanai and Kelvin waves in Fig. 2(a) thus have their origin in topology, just as they do for the shallow water equations using an f-plane approximation [1].

C. Sinusoidal horizontal shear

Next, we find the winding number of the Poincaré modes in the shallow water equations subjected to the sinusoidal horizontal shear. Figure 11 shows the phase of $\Xi_\pm(\mathbf{k})$ for $U_0 = 0.3$ and constant Coriolis parameter $f_0 = \pm 1$ showing qualitatively similiar vortices as those in Fig. 9. Again the positive frequency Poincaré modes exhibit a vortex for $f_0 > 0$ and an anti-vortex for $f_0 < 1$ at the origin in wave-vector space (the phase singularity is absent for the planetary modes). The change in the winding number of 2 is consistent with the number of edge modes seen in the spectrum [Figs. 2(b) and 2(c)]. This result suggests that the localized Kelvin and Yanai modes that traverse the gap between Rossby modes and the bulk Poincaré modes have a topological origin like the equatorial modes in the absence of shear. This is the main result of the paper, and we note that the result also holds in perturbation theory with the 9×9 linear wave operator, as the perturbative corrections to the wave function do not alter the winding number. The appearance of Kelvin and Yanai waves along the equators shown in Sec. III A is thus consistent with the persistence of the bulk-interface correspondence in the presence of shear.

Finally, we study the phase of the gauge-invariant quantity $\Xi_\pm(\mathbf{k})$ for the linearized primitive equations with and

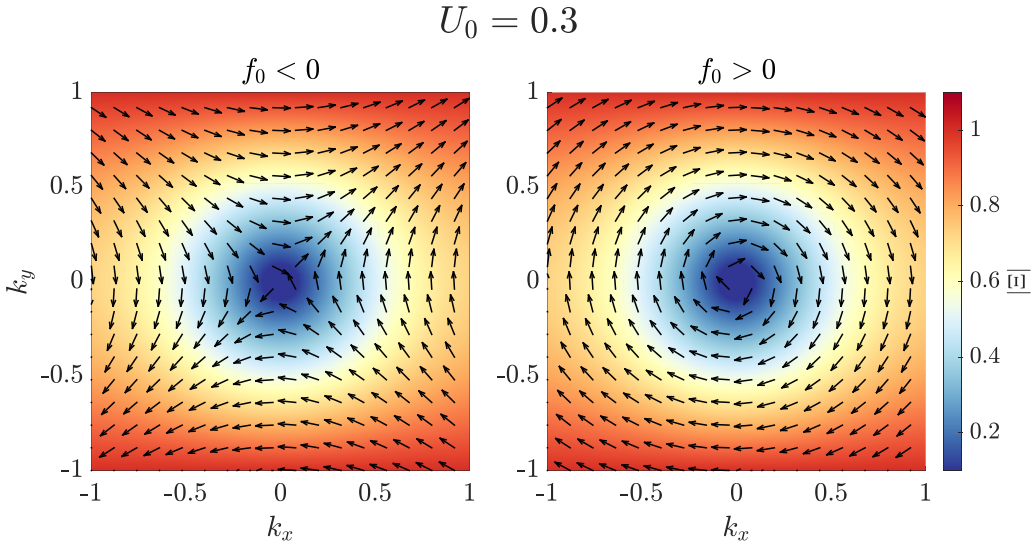

FIG. 11. Same as Fig. 9 but for the lowest positive frequency Poincaré modes as indicated by the direction of the arrows for the case of sinusoidal horizontal shear $U_0 = 0.3$ within the f-plane approximation for $f_0 = -1$ (left) and $f_0 = 1$ (right) with $L_y \to \infty$. Colors represent normalized magnitude $|\Xi|$ in arbitrary units.

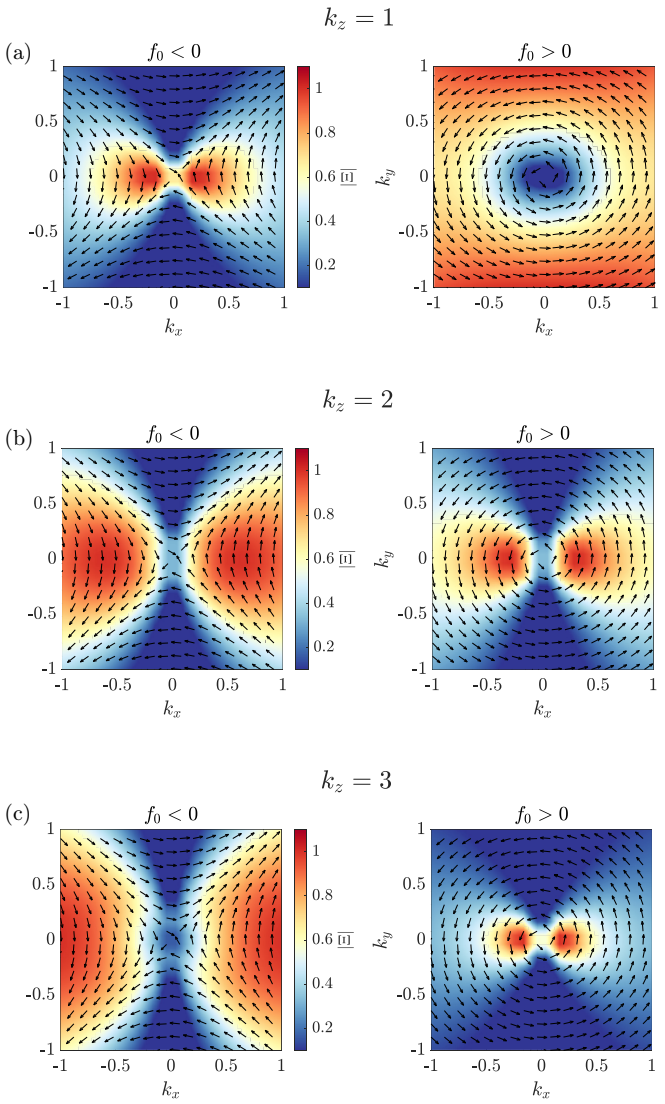

FIG. 12. Same as Fig. 9 but for a positive Poincaré mode with a linear vertical shear flow with $U_0 = 0.05$ within the f-plane approximation for $f_0 = -1$ (left) and $f = 1$ (right). (a) $k_z = 1$, (b) $k_z = 2$, (c) $k_z = 3$. Obtained using DEDALUS with $N_z = 20$ and $L_z = 2\pi$ using a Fourier basis.

without forcing from sinusoidal horizontal shear. The phase singularity of $\Xi_{\pm}(\mathbf{k})$ for primitive equations (not shown) is similar to that depicted in Figs. 9 and 11. Without shear, the positive and negative frequency Poincaré modes have opposing winding numbers, and the winding number also changes polarity when f changes signs, in agreement with the analytic calculation of the Chern number. The vortex of the bulk Poincaré modes continues to be robust in the presence of shear, despite the combined effects of broken translational invariance, non-Hermiticity, and instability. We have verified that the dispersion relation of the shear-forced primitive equations on the planet with two equators continues to exhibit spectral flow of the Kelvin and Yanai waves across the band gaps.

D. Linear vertical shear

We proceed to calculate the winding number of the Poincaré modes in the primitive equators subject to the linear vertical shear flow. Primitive equations with a vertical shear flow $U(z)$ are given as Eq. (27), which we simulate using DEDALUS. Figure 12 shows that in the presence of linear vertical shear flow, the bulk Poincaré mode exhibits phase singularity, and the winding number depends on the sign of the Coriolis parameters for all vertical wave numbers k_z's. This suggests that the Yanai and Kelvin waves in Fig. 6 are topologically nontrivial. Note that while Fig. 12 is obtained with a Fourier basis and thus the effect of the rigid-lid boundary is removed, we verified that the winding numbers are similar to Fig. 12 with a no-slip boundary condition using a Chebyshev basis for each coefficient. Therefore, the topological nature of the boundary waves is robust against the presence of the Eady instability.

VII. DISCUSSION AND CONCLUSION

We investigated the topological properties of rotating shallow water equations and stratified primitive equations in the presence of shear flow that breaks translational invariance in the meridional direction and Hermiticity and introduces instabilities. The winding number of the phase of $\Xi_{\pm}(\mathbf{k})$ serves as a convenient probe of topological properties of the wave functions. This alternative to calculating the Chern number remains computationally tractable in the absence of translational invariance and Hermiticity. It may find applications to experimental and observational data as well as to idealized theoretical models such as those studied here, as it can be obtained from the (usually neglected) phase information of the cross-periodogram between different fields such as the zonal velocity and geopotential height. To verify that the method yields sensible results, we studied the bulk modes in the presence of a spatially varying Coriolis parameter that does not change signs and demonstrated consistency with the standard calculation of the Chern number on the f plane [1]. An alternative and equivalent way of quantifying the topological invariant is through the spectral index by counting the number of upward-going eigenvectors for increasing momentum, which is useful when we have access to the wave function [46,63].

Our main result is that the winding number for both the shallow water equations and primitive equations remains unchanged in the presence of forcing by background shear flow. The difference in the winding number of the Poincaré bands on opposite sides of the equator matches with the number of unidirectional waves localized at the equator, consistent with a topological origin for these forced Kelvin and Yanai waves. For the stratified primitive equations, there are topologically protected modes at each allowed vertical wave number in analogy to the physics of weak three-dimensional topological insulators.

We note that we do not rigorously prove the bulk-interface correspondence for the shear flows, nor topological protection. However, we show that the bulk spectrum in f-plane approximation evolves smoothly with increasing U_0 and the

phase singularities persist in both the numerically found eigenmodes and in low-order perturbation theory, at least if U_0 is not too large. It may be possible to generalize the approach taken in Ref. [64] for frictionally damped shallow water waves to the problem of background shear. That system, and the problems investigated here, are invariant under the combined operation of parity and time reversal (PT). We leave this, and an investigation of the maximum shear that will support equatorial waves of topological origin, for future work.

ACKNOWLEDGMENTS

We thank D. Borgnia, D. Carmichael, D. Nguyen, S. Tobias, and A. Venaille for helpful discussions. Z.Z. is supported by the STC Center for Integrated Quantum Materials, NSF Grant No. DMR-1922172, ARO MURI Grant No. W911NF14-0247, NSF DMREF Grant No. 1922165, and a Stanford Science fellowship. J.B.M. is supported in part by a grant from the Simons Foundation (Grant No. 662962, GF) and by U.S. National Science Foundation Grants No. OIA-1921199.

APPENDIX A: LINEARIZED SHALLOW WATER EQUATIONS IN THE PRESENCE OF HORIZONTAL SHEAR

We begin with the nonlinear shallow-water equations in the presence of rotation,

$$\frac{\partial \boldsymbol{u}_{\rm tot}}{\partial t} + (\boldsymbol{u}_{\rm tot}\cdot\boldsymbol{\nabla})\boldsymbol{u}_{\rm tot} = -g\boldsymbol{\nabla}h - \boldsymbol{f}\times\boldsymbol{u}_{\rm tot},$$
$$\frac{\partial h}{\partial t} + \boldsymbol{\nabla}\cdot(h\boldsymbol{u}_{\rm tot}) = 0, \tag{A1}$$

where $\boldsymbol{u}_{\rm tot} = \boldsymbol{u} + \boldsymbol{U}$, $\boldsymbol{u} = (u, v)$, $\boldsymbol{U} = (U(y), 0)$ is the shear flow along the zonal direction, $\boldsymbol{f} = f(y)\hat{z}$ is the Coriolis parameter, and $h = \eta + H(y)$. To the linear order, Eq. (A1) can be written as follows:

$$\frac{\partial u}{\partial t} + U(y)\frac{\partial u}{\partial x} + v\frac{\partial U(y)}{\partial y} + g\frac{\partial \eta}{\partial x} - f(y)v = 0,$$
$$\frac{\partial v}{\partial t} + U(y)\frac{\partial v}{\partial x} + g\frac{\partial \eta}{\partial y} + f(y)u = 0,$$
$$\frac{\partial \eta}{\partial t} + H(y)\left(\frac{\partial u}{\partial x} + \frac{\partial v}{\partial y}\right) + v\frac{\partial H(y)}{\partial y} + U(y)\frac{\partial \eta}{\partial x} = 0. \tag{A2}$$

A deformation length scale L_d and gravity wave speed c are defined to be

$$L_d \equiv \frac{c}{2\Omega}, \quad c \equiv \sqrt{gH}, \tag{A3}$$

where H is the zonally averaged depth without shear [$H(y) = H + h(y)$]. Introducing the dimensionless quantities $\tilde{t} = 2\Omega t$, $\tilde{\eta} = \frac{\eta}{H}$, $\tilde{H}(y) = 1 + \frac{h(y)}{H}$, $\tilde{\boldsymbol{u}} = \frac{\boldsymbol{u}}{c}$, $\boldsymbol{U} = \frac{U}{c}$, $\tilde{f}(y) = \frac{f(y)}{2\Omega}$, and $\tilde{\boldsymbol{x}} = \frac{\boldsymbol{x}}{L_d}$, the linearized equations of motion [Eq. (A2)] around the basic state ($\boldsymbol{u} = 0, h = H$) can then be written as follows:

$$\partial_{\tilde{t}}\tilde{u} + \tilde{U}(y)\partial_{\tilde{x}}\tilde{u} + \tilde{v}\partial_{\tilde{y}}\tilde{U}(y) + \partial_{\tilde{x}}\tilde{\eta} - \tilde{f}(y)\tilde{v} = 0,$$
$$\partial_{\tilde{t}}\tilde{v} + \tilde{U}(y)\partial_{\tilde{x}}\tilde{v} + \partial_{\tilde{y}}\tilde{\eta} + \tilde{f}(y)\tilde{u} = 0,$$
$$\partial_{\tilde{t}}\tilde{\eta} + \tilde{H}(y)(\partial_{\tilde{x}}\tilde{u} + \partial_{\tilde{y}}\tilde{v}) + \tilde{v}\partial_{\tilde{y}}\tilde{H}(y) + \tilde{U}(y)\partial_{\tilde{x}}\tilde{\eta} = 0. \tag{A4}$$

For convenience, we drop the tilde in the main text.

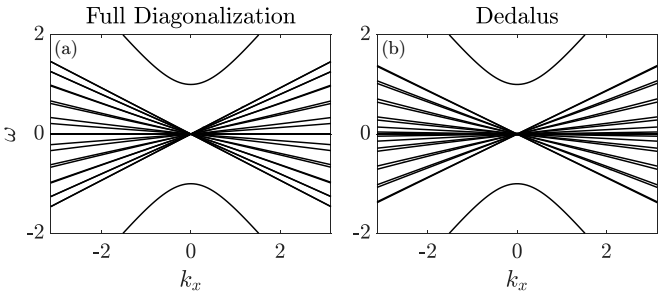

FIG. 13. Frequency spectra of the shallow water equations in the f-plane approximation with $f = 1$ and subjected to sine shear $U_0 = 0.5$. The frequencies are obtained by (a) diagonalizing the 69×69 wave-vector space linear wave operator and from (b) DEDALUS with $N_y = 23$.

APPENDIX B: THE SHALLOW WATER LINEAR WAVE OPERATOR IN WAVE-VECTOR SPACE

The matrix elements of the linear wave operator Eq. (16) in wave-vector space may be written using Dirac braket notation as $\langle k_x', k_y'|\hat{L}|k_x, k_y\rangle$. Since the linear wave operator has no dependence on x, these matrix elements are nonzero only for $k_x' = k_x$. Along the y direction, we make use of the following relations:

$$\frac{1}{L_y}\int_{-L_y/2}^{L_y/2} dy\, \sin\left(\frac{2\pi y}{\Lambda}\right) e^{i(k_y'-k_y)y}$$
$$= \frac{1}{2i}[\delta_{k_y',k_y-2\pi/\Lambda} - \delta_{k_y',k_y+2\pi/\Lambda}], \tag{B1}$$

and

$$\frac{1}{L_y}\int_{-L_y/2}^{L_y/2} dy\, \cos\left(\frac{2\pi y}{\Lambda}\right) e^{i(k_y'-k_y)y}$$
$$= \frac{1}{2}[\delta_{k_y',k_y-2\pi/\Lambda} + \delta_{k_y',k_y+2\pi/\Lambda}]. \tag{B2}$$

In the absence of shear ($U_0 = 0$), the linear wave operator in k space is a block-diagonal matrix, with the diagonal blocks being $L_0(k_x, k_y, f)$ and with no off-diagonal blocks. The 3×3 linear wave operators L_0 at wave vectors (k_x, k_y) and $(k_x, k_y \pm 2\pi)$ are connected by the sinusoidal horizontal shear as a wave at wave vector k_y mixes with modes $k_y' = k_y \pm 2\pi$. For a given k_x, we need to diagonalize the full matrix in the basis of $k_y, k_y \pm 2\pi, k_y \pm 4\pi, \ldots$, imposing a finite cutoff in $|k_y'|$ to keep the dimension of the matrix finite.

APPENDIX C: COMPARISON WITH DEDALUS

We validate our diagonalization scheme by comparing with DEDALUS [50]. Figure 13 compares the spectra from diagonalizing a 69×69 linear wave operator corresponding to the 23 retained wave vectors in the y direction with the spectrum obtained from DEDALUS. To enable the comparison, the linear wave operator has been truncated to finite dimension in wave-number space to match the total number of equations in DEDALUS. The full diagonalization captures both the spread of the geostrophic modes and the bulk Poincaré modes. Note that the small difference in the geostrophic modes is due to the fact that the sample points along the y direction in DEDALUS is

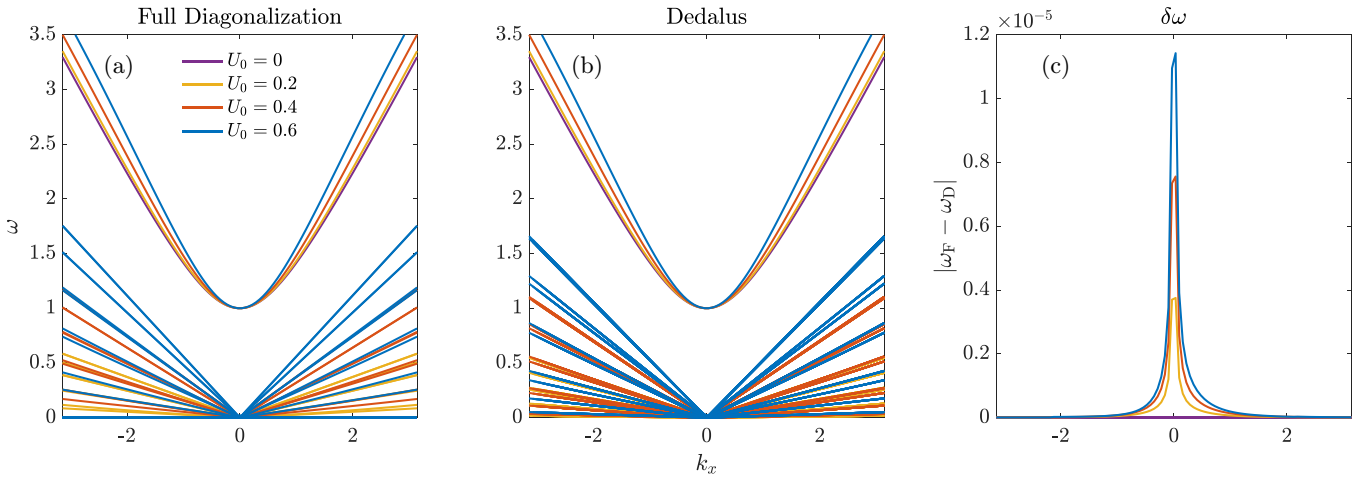

FIG. 14. Comparison of the frequencies of the positive Poincaré and planetary modes. (a) Full diagonalization of the 69×69 linear wave operator. (b) DEDALUS with $N_y = 23$. (c) The difference between frequencies of the lowest positive Poincaré mode obtained from full diagonalization, ω_F, and Dedalus, ω_D in (a) and (b).

nonuniform whereas in the direct diagonalization, k_y's are sampled uniformly. Figure 14 compares the positive frequency modes obtained from full diagonalization versus those found using DEDALUS. The two methods show excellent agreement. The frequency of the Poncaré modes increases with increasing shear and remain distinct beyond $U_0 = 0.6$. We can apply the same procedure to obtain the transition matrices T_1 and T_2 for the cosine shear, and the spectra agrees with Figs. 13 and 14, as expected.

APPENDIX D: PRIMITIVE EQUATIONS

Using the same nondimensionalization as Appendix A, the nondimensional Boussinesq primitive equations are given as follows [5]:

$$\begin{aligned} R_0\frac{D\boldsymbol{u}}{Dt} + \boldsymbol{f}(y)\times\boldsymbol{u} &= -\nabla\phi,\\ R_0\frac{Db}{Dt} + \left(\frac{L_d}{L_y}\right)^2 N^2 w &= 0,\\ \partial_z\phi &= b,\\ \partial_x u + \partial_y v + \partial_z w &= 0, \end{aligned} \tag{D1}$$

where w is the vertical velocity, ϕ is the kinetic pressure, and b is the buoyancy fluctuation about an average stratification, $N^2 = \partial b/\partial z$, and L_d is the deformation radius, and R_0 is the Rossby number. We consider the linearized equations

$$\begin{aligned} R_0\frac{\partial\boldsymbol{u}}{\partial t} + \boldsymbol{f}(y)\times\boldsymbol{u} &= -\nabla\phi,\\ R_0\frac{\partial b}{\partial t} + \left(\frac{L_d}{L_y}\right)^2 N^2 w &= 0,\\ \partial_z\phi &= b,\\ \partial_x u + \partial_y v + \partial_z w &= 0. \end{aligned} \tag{D2}$$

Here, R_0 and NL_d/L_y can be set to unity by appropriate rescaling of the variables. In the Fourier space, $-ik_z\phi = b$ and $ik_x u + ik_y v + ik_z w = 0$. Therefore, we can eliminate ϕ and w by writing them in terms of b, u, and v. In the f-plane approximation, the dispersion relation for the Poincaré modes is $\omega^2 = f^2 + (k_x^2 + k_y^2)/k_z^2$.

Finally, we consider the imposition of sinusoidal horizontal shear flow. We assume the system is periodic in the zonal and meridional directions and has rigid lids at $z = 0$ and $z = L_z$, where L_z is a constant. Let $\boldsymbol{u}_{\rm tot} = \boldsymbol{u} + \boldsymbol{U}$, $\boldsymbol{u} = (u, v)$, $\boldsymbol{U} = (U(y), 0)$ and $\phi = \eta + H(y)$. From geostrophic balance, $U(y)$ and $H(y)$ must satisfy Eq. (5). Substituting $\boldsymbol{u}_{\rm tot}$ and ϕ into Eq. (D1) and discarding nonlinear terms, we obtain

$$\begin{aligned} \frac{\partial u}{\partial t} &= -U(y)\frac{\partial u}{\partial x} - v\frac{\partial U(y)}{\partial y} + \frac{f(y)}{R_0}v - \frac{1}{R_0}\frac{\partial\eta}{\partial x},\\ \frac{\partial v}{\partial t} &= -\frac{f(y)}{R_0}u - U(y)\frac{\partial v}{\partial x} - \frac{1}{R_0}\frac{\partial\eta}{\partial y},\\ \frac{\partial}{\partial t}\frac{\partial\eta}{\partial z} &= -\frac{1}{R_0}\left(\frac{L_d}{L_y}\right)^2 N^2 w - U(y)\frac{\partial^2}{\partial x\partial z}\eta. \end{aligned} \tag{D3}$$

Again, R_0 and $N^2(L_d/L_y)^2$ may be set to unity. By doing so, Eq. (D3) simplifies to

$$\begin{aligned} \frac{\partial u}{\partial t} &= -U(y)\frac{\partial u}{\partial x} - v\frac{\partial U(y)}{\partial y} + f(y)v - \frac{\partial\eta}{\partial x},\\ \frac{\partial v}{\partial t} &= -f(y)u - U(y)\frac{\partial v}{\partial x} - \frac{\partial\eta}{\partial y},\\ \frac{\partial}{\partial t}\frac{\partial\eta}{\partial z} &= -w - U(y)\frac{\partial^2}{\partial x\partial z}\eta. \end{aligned} \tag{D4}$$

[1] P. Delplace, J. B. Marston, and A. Venaille, Topological origin of equatorial waves, Science **358**, 1075 (2017).

[2] A. Venaille and P. Delplace, Wave topology brought to the coast, Phys. Rev. Res. **3**, 043002 (2021).

[3] W. Thomson, On gravitational oscillations of rotating water, Proc. R. Soc. Edinburgh **10**, 92 (1880).

[4] W. Xu, B. Fox-Kemper, J.-E. Lee, J. Marston, and Z. Zhu, Topological signature of stratospheric poincare–gravity waves, arXiv:2306.12191.

[5] G. K. Vallis, *Atmospheric and Oceanic Fluid Dynamics,* 2nd ed. (Cambridge University Press, Cambridge, UK, 2017).

[6] M. Hammond and R. T. Pierrehumbert, Wave-mean flow interactions in the atmospheric circulation of tidally locked planets, Astrophys. J. **869**, 65 (2018).

[7] W. V. R. Malkus, Outline of a theory of turbulent shear flow, J. Fluid Mech. **1**, 521 (1956).

[8] B. D. Fried, M. Gell-Mann, J. D. Jackson, and H. W. Wyld, Longitudinal plasma oscillations in an electric field, J. Nucl. Energy Part C **1**, 190 (1960).

[9] J. R. Herring, Investigation of problems in thermal convection, J. Atmos. Sci. **20**, 325 (1963).

[10] M. Z. Hasan and C. L. Kane, Colloquium: Topological insulators, Rev. Mod. Phys. **82**, 3045 (2010).

[11] X.-L. Qi and S.-C. Zhang, Topological insulators and superconductors, Rev. Mod. Phys. **83**, 1057 (2011).

[12] Z. Wang, Y. Chong, J. D. Joannopoulos, and M. Soljačić, Observation of unidirectional backscattering-immune topological electromagnetic states, Nature **461**, 772 (2009).

[13] Y. Plotnik, M. C. Rechtsman, D. Song, M. Heinrich, J. M. Zeuner, S. Nolte, Y. Lumer, N. Malkova, J. Xu, A. Szameit, Z. Chen, and M. Segev, Observation of unconventional edge states in "photonic graphene," Nat. Mater. **13**, 57 (2014).

[14] S. A. Skirlo, L. Lu, and M. Soljačić, Multimode One-Way Waveguides of Large Chern Numbers, Phys. Rev. Lett. **113**, 113904 (2014).

[15] S. A. Skirlo, L. Lu, Y. Igarashi, Q. Yan, J. Joannopoulos, and M. Soljačić, Experimental Observation of Large Chern Numbers in Photonic Crystals, Phys. Rev. Lett. **115**, 253901 (2015).

[16] V. Peano, C. Brendel, M. Schmidt, and F. Marquardt, Topological Phases of Sound and Light, Phys. Rev. X **5**, 031011 (2015).

[17] Z. Yang, F. Gao, X. Shi, X. Lin, Z. Gao, Y. Chong, and B. Zhang, Topological Acoustics, Phys. Rev. Lett. **114**, 114301 (2015).

[18] C. He, X. Ni, H. Ge, X.-C. Sun, Y.-B. Chen, M.-H. Lu, X.-P. Liu, and Y.-F. Chen, Acoustic topological insulator and robust one-way sound transport, Nat. Phys. **12**, 1124 (2016).

[19] L. M. Nash, D. Kleckner, A. Read, V. Vitelli, A. M. Turner, and W. T. M. Irvine, Topological mechanics of gyroscopic metamaterials, Proc. Natl. Acad. Sci. USA **112**, 14495 (2015).

[20] S. D. Huber, Topological mechanics, Nat. Phys. **12**, 621 (2016).

[21] M. G. Silveirinha, Chern invariants for continuous media, Phys. Rev. B **92**, 125153 (2015).

[22] S. Shankar, M. J. Bowick, and M. C. Marchetti, Topological Sound and Flocking on Curved Surfaces, Phys. Rev. X **7**, 031039 (2017).

[23] R. Green, J. Armas, J. de Boer, and L. Giomi, Topological waves in passive and active fluids on curved surfaces: a unified picture, arXiv:2011.12271.

[24] J. B. Parker, J. B. Marston, S. M. Tobias, and Z. Zhu, Topological Gaseous Plasmon Polariton in Realistic Plasma, Phys. Rev. Lett. **124**, 195001 (2020).

[25] J. B. Parker, J. W. Burby, J. B. Marston, and S. M. Tobias, Nontrivial topology in the continuous spectrum of a magnetized plasma, Phys. Rev. Res. **2**, 033425 (2020).

[26] Y. Fu and H. Qin, Topological phases and bulk-edge correspondence of magnetized cold plasmas, Nat. Commun. **12**, 3924 (2021).

[27] Y. E. Kraus, Y. Lahini, Z. Ringel, M. Verbin, and O. Zilberberg, Topological States and Adiabatic Pumping in Quasicrystals, Phys. Rev. Lett. **109**, 106402 (2012).

[28] M. Lohse, C. Schweizer, O. Zilberberg, M. Aidelsburger, and I. Bloch, A Thouless quantum pump with ultracold bosonic atoms in an optical superlattice, Nat. Phys. **12**, 350 (2016).

[29] M. A. Bandres, S. Wittek, G. Harari, M. Parto, J. Ren, M. Segev, D. N. Christodoulides, and M. Khajavikhan, Topological insulator laser: Experiments, Science **359**, eaar4005 (2018).

[30] O. Zilberberg, S. Huang, J. Guglielmon, M. Wang, K. P. Chen, Y. E. Kraus, and M. C. Rechtsman, Photonic topological boundary pumping as a probe of 4D quantum Hall physics, Nature **553**, 59 (2018).

[31] R. P. Pedro, J. Paulose, A. Souslov, M. Dresselhaus, and V. Vitelli, Topological Protection Can Arise from Thermal Fluctuations and Interactions, Phys. Rev. Lett. **122**, 118001 (2019).

[32] H. Shen, B. Zhen, and L. Fu, Topological Band Theory for Non-Hermitian Hamiltonians, Phys. Rev. Lett. **120**, 146402 (2018).

[33] Z. Gong, Y. Ashida, K. Kawabata, K. Takasan, S. Higashikawa, and M. Ueda, Topological Phases of Non-Hermitian Systems, Phys. Rev. X **8**, 031079 (2018).

[34] H. Zhou and J. Y. Lee, Periodic table for topological bands with non-Hermitian symmetries, Phys. Rev. B **99**, 235112 (2019).

[35] D. S. Borgnia, A. J. Kruchkov, and R.-J. Slager, Non-Hermitian boundary Modes and Topology, Phys. Rev. Lett. **124**, 056802 (2020).

[36] T. E. Lee, Anomalous Edge State in a Non-Hermitian Lattice, Phys. Rev. Lett. **116**, 133903 (2016).

[37] Y. Xiong, Why does bulk boundary correspondence fail in some non-Hermitian topological models, J. Phys. Commun. **2**, 035043 (2018).

[38] S. Yao and Z. Wang, Edge States and Topological Invariants of Non-Hermitian Systems, Phys. Rev. Lett. **121**, 086803 (2018).

[39] F. K. Kunst, E. Edvardsson, J. C. Budich, and E. J. Bergholtz, Biorthogonal Bulk-Boundary Correspondence in Non-Hermitian Systems, Phys. Rev. Lett. **121**, 026808 (2018).

[40] C. Yin, H. Jiang, L. Li, R. Lü, and S. Chen, Geometrical meaning of winding number and its characterization of topological phases in one-dimensional chiral non-Hermitian systems, Phys. Rev. A **97**, 052115 (2018).

[41] T. Helbig, T. Hofmann, S. Imhof, M. Abdelghany, T. Kiessling, L. W. Molenkamp, C. H. Lee, A. Szameit, M. Greiter, and R. Thomale, Generalized bulk-boundary correspondence in non-Hermitian topolectrical circuits, Nat. Phys. **16**, 747 (2020).

[42] L. Xiao, T. Deng, K. Wang, G. Zhu, Z. Wang, W. Yi, and P. Xue, Non-Hermitian bulk-boundary correspondence in quantum dynamics, Nat. Phys. **16**, 761 (2020).

[43] A. Ghatak, M. Brandenbourger, J. van Wezel, and C. Coulais, Observation of non-Hermitian topology and its bulk-edge correspondence in an active mechanical metamaterial, Proc. Natl. Acad. Sci. USA **117**, 29561 (2020).

[44] D. J. Thouless, M. Kohmoto, M. P. Nightingale, and M. den Nijs, Quantized Hall Conductance in a Two-Dimensional Periodic Potential, Phys. Rev. Lett. **49**, 405 (1982).

[45] M. Z. Hasan and J. E. Moore, Three-dimensional topological insulators, Annu. Rev. Condens. Matter Phys. **2**, 55 (2011).

[46] F. Faure, Manifestation of the topological index formula in quantum waves and geophysical waves, Ann. Henri Lebesg. **6**, 449 (2023).

[47] J. B. Parker, Topological phase in plasma physics, J. Plasma Phys. **87**, 835870202 (2021).

[48] S. A. R. Horsley, Tutorial topology, waves, and the refractive index, Int. J. Theor. Phys. **62**, 135 (2023).

[49] O. Bühler, *Waves and Mean Flows* (Cambridge University Press, Cambridge, UK, 2014).

[50] K. J. Burns, G. M. Vasil, J. S. Oishi, D. Lecoanet, and B. P. Brown, Dedalus: A flexible framework for numerical simulations with spectral methods, Phys. Rev. Res. **2**, 023068 (2020).

[51] G. Brunet and T. Warn, Rossby wave critical layers on a jet, J. Atmos. Sci. **47**, 1173 (1990).

[52] Y. Fu and H. Qin, The physics of spontaneous parity-time symmetry breaking in the Kelvin-Helmholtz instability, New J. Phys. **22**, 083040 (2020).

[53] T. W. David, P. Delplace, and A. Venaille, How do CPT-like symmetries shape the stability of geophysical flows? arXiv:2112.09511.

[54] M. M. Sternheim and J. F. Walker, Non-Hermitian Hamiltonians, decaying states, and perturbation theory, Phys. Rev. C **6**, 114 (1972).

[55] C. Buth, R. Santra, and L. S. Cederbaum, Non-Hermitian Rayleigh-Schrödinger perturbation theory, Phys. Rev. A **69**, 032505 (2004).

[56] J. P. Boyd, The effects of latitudinal shear on equatorial waves. Part I: Theory and methods, J. Atmos. Sci. **35**, 2236 (1978).

[57] M. Perrot, P. Delplace, and A. Venaille, Topological transition in stratified fluids, Nature **15**, 781 (2019).

[58] P. Ripa, General stability conditions for zonal flows in a one-layer model on the beta-plane or the sphere, J. Fluid Mech. **126**, 463 (1983).

[59] Y. Hatsugai, Chern Number and Edge States in the Integer Quantum Hall Effect, Phys. Rev. Lett. **71**, 3697 (1993).

[60] Z. F. Wang, K.-H. Jin, and F. Liu, Quantum spin Hall phase in 2D trigonal lattice, Nat. Commun. **7**, 12746 (2016).

[61] T. Fösel, V. Peano, and F. Marquardt, L lines, C points and Chern numbers: Understanding band structure topology using polarization fields, New J. Phys. **19**, 115013 (2017).

[62] P. Bouteyre, D. X. Nguyen, G. Gachon, T. Benyattou, X. Letartre, P. Viktorovitch, S. Callard, L. Ferrier, and H. S. Nguyen, Non-Hermitian topological invariant of photonic band structures undergoing inversion, arXiv:2211.09884.

[63] A. Venaille, Y. Onuki, N. Perez, and A. Leclerc, From ray tracing to waves of topological origin in continuous media, SciPost Phys. **14**, 062 (2023).

[64] P. Delplace, T. Yoshida, and Y. Hatsugai, Symmetry-Protected Multifold Exceptional Points and Their Topological Characterization, Phys. Rev. Lett. **127**, 186602 (2021).